 doi:10.20944/preprints202106.0539.v1

*Article*

# Improving the CO and $CH_4$ gas sensor response at room temperature of $\alpha$-$Fe_2O_3$(0001) epitaxial thin films grown on $SrTiO_3$(111) incorporating Au(111) islands

**Aida Serrano[1,2,3,*], Jesús López-Sánchez[2,3,4], Iciar Arnay[2,3], Rosalia Cid[2,3], María Vila[2,3,5], Eduardo Salas-Cólera[2,3] and Germán R. Castro[2,3] and Juan Rubio-Zuazo[2,3]**

[1] Instituto de Cerámica y Vidrio (ICV), CSIC, 28049 Madrid, Spain
[2] Spanish CRG BM25-SpLine at The ESRF - The European Synchrotron, 38000 Grenoble, France
[3] Instituto de Ciencia de Materiales de Madrid (ICMM), CSIC, 28049 Madrid, Spain
[4] Departamento de Física de Materiales, Universidad Complutense de Madrid, 28040 Madrid, Spain
[5] Escuela Técnica Superior de Ingeniería de Telecomunicación (ETSIT), Universidad Rey Juan Carlos, 28933 Madrid, Spain
* Correspondence: aida.serrano@csic.es

**Abstract:** In this work epitaxial Au islands have been grown on epitaxial $\alpha$-$Fe_2O_3$ thin film by pulsed laser deposition on $SrTiO_3$(111) substrate. Both Au and $\alpha$-$Fe_2O_3$ layer show an island-type growth with an average particle size of 42 and 60 nm, respectively. The crystallographic coupling of lattices is confirmed with a rotation of 30º between the in-plane crystallographic axes of $\alpha$-$Fe_2O_3$ structure and those of $SrTiO_3$(111) substrate and between the in-plane crystallographic axes of Au and those of $\alpha$-$Fe_2O_3$ structure. $\alpha$-$Fe_2O_3$ is the only phase of iron oxide identified before and after its functionalization with Au nanoparticles. In addition, its structural characteristics are also preserved after Au deposition, with minor changes at short-range. The functional character of the complex systems as gas sensor has been proven. Conductance measurements of Au(111)/$\alpha$-$Fe_2O_3$(0001)/ $SrTiO_3$(111) system show that the incorporation of Au islands on top of the $\alpha$-$Fe_2O_3$(0001) layer induces an enhancement of the gas-sensing activity at room temperature for CO and $CH_4$ gas in comparison to a bare $\alpha$-$Fe_2O_3$(0001) layer grown on $SrTiO_3$(111).

**Keywords:** Au/$\alpha$-$Fe_2O_3$ system; island-type growth; epitaxial growth; surface functionalization; gas sensor activity

## 1. Introduction

$\alpha$-$Fe_2O_3$ (hematite) is one of the most abundant mineral and probably one of the most used iron oxide due to its interesting properties such as its low toxicity, stability under ambient conditions and low costs [1–3]. Its morphological forms can be assorted controlling the physical properties, which allows employing this iron oxide polymorph in different fields as magnetic data storage technologies, biomedicine, catalysis or gas sensors [1,4–8], demonstrating its high-potential. For example, for water splitting applications $\alpha$-$Fe_2O_3$ has been considered as an active oxide for CO oxidation at low temperature [9,10]. In addition, a larger photochemical reactivity has been identified in $\alpha$-$Fe_2O_3$ surfaces grown on $SrTiO_3$(111) substrates [11]. As gas sensor for monitoring combustible or toxic gases, $\alpha$-$Fe_2O_3$ has been also continuously investigated. Mesoporous nanoparticles, nanoporous nanoparticles, hollow balls, thin films and single-crystalline oblique nanoparallelepipeds, among others, are some of the configurations employed with reported gas sensing properties [12–18].

The incorporation of certain nanoparticles on active surfaces allows enhancing their physical properties for a wide range of attractive applications. In this respect, the func-

tionalization of $\alpha$-$Fe_2O_3$ surfaces with noble metallic nanoparticles has been proven to improve, for example, the catalytic activities [19–21]. However, the transfer of this type of nanoparticles, without modifying their characteristics and properties, is not an easy way and considerable efforts have been expended on it. A common and interesting approach that allows covering large surfaces with functional nanoparticles is the solid state dewetting [22–25]. Based on this processing method, a one-step strategy has been reported in which noble metal nanostructures are prepared on an oxide support by the deposition of metallic material with the substrate at a specific temperature [26–28]. This approach avoids a subsequent annealing process after the deposition of a metallic film [22–24,29] and to the best of our knowledge it has been used to obtain Au and Pt nanoparticles on iron oxide surfaces [26,28] and Al nanostructures on Si and glass substrates [27]. Using this methodology, recently we have investigated the effect of the substrate temperature and the type of the substrate in the preparation of Au nanostructures on $\alpha$-$Fe_2O_3$ surfaces, reporting a precise control of the morphological characteristics of the noble metal nanostructures tuning accurately the growth parameters [28].

In this work, considering these premises, we have studied the incorporation of Au nanoparticles on $\alpha$-$Fe_2O_3$ thin films grown on $SrTiO_3$(111) and the gas-sensing properties of the complex systems. An exhaustive morphological and structural characterization of $\alpha$-$Fe_2O_3$/$SrTiO_3$(111) and Au/$\alpha$-$Fe_2O_3$/$SrTiO_3$(111) heterostructures has been carried out examining the $\alpha$-$Fe_2O_3$ structure before and after its surface functionalization with Au islands. In addition, conductance experiments are presented, showing the enhancement of the gas-sensing performance of the functionalized epitaxial $\alpha$-$Fe_2O_3$ layers when epitaxial Au nanostructures are incorporated on top.

## 2. Materials and Methods

$\alpha$-$Fe_2O_3$ thin films and Au nanoparticles/$\alpha$-$Fe_2O_3$ heterostructures were grown on $SrTiO_3$ (STO)(111) substrates by pulsed laser deposition according to a previous work [28]. The growth was performed by using an ultraviolet pulsed laser source (355 nm) of high power (1 W) to obtain the plasma, with a base pressure of $10^{-9}$ mbar. $\alpha$-$Fe_2O_3$ thin films were deposited with the substrates at 400 ºC using an $\alpha$-$Fe_2O_3$ target under an $O_2$ atmosphere ($P_{O2}$ of $10^{-4}$ mbar), while Au nanoparticles were grown from a Au target on $\alpha$-$Fe_2O_3$ films keeping the oxygen pressure $P_{O2}$ about $10^{-4}$ mbar, in order to prevent the reduction to $Fe_3O_4$, and with the sample at 250 ºC.

During the deposition process, the crystalline character of both layers was analyzed by *in-situ* reflection high-energy electron diffraction (RHEED) using a primary electron-beam of 29 keV. Morphology of the samples was studied by scanning electron microscopy (SEM) with an S-4700 Hitachi instrument at 20 kV and morphological features were examined by using the software ImageJ.

Grazing incidence X-ray diffraction (GIXRD), X-ray reflectivity (XRR) and X-ray absorption spectroscopy (XAS) experiments were carried out at the Spanish CRG synchrotron beamline BM25-SpLine at the European Synchrotron Radiation Facility (ESRF), in Grenoble (France). GIXRD and XRR measurements were carried out in a high precision six-circle diffractometer in vertical geometry [30] at room temperature using a photon wavelength of 0.826 Å (hν= 15 keV) to ensure the access to a wide reciprocal space region. XAS experiments were performed at the Fe K-edge (7112 eV) at room temperature in fluorescence mode using a 13-elements Si(Li) detector located 90º respect to the incoming X-ray beam. Spectra of reference standards (Fe foil, FeO, $Fe_3O_4$ and $\alpha$-$Fe_2O_3$) were measured for comparison in transmission mode with two ionization chambers as detectors. XAS data were analysed using Demeter package [31,32].

X-ray photoelectron spectroscopy (XPS) measurements were carried out on the Fe 2p and Au 4f core level using a standard monochromatic X-ray tube with a Mg K$\alpha$ radiation anode (hν = 1253.6 eV). The binding energy of XPS spectra was calibrated considering the C1s binding energy of a small residual amount as 284.8 eV.

 doi:10.20944/preprints202106.0539.v1



The gas sensing characteristics of the samples were measured in a home-made chamber for CO and $CH_4$ gas at room temperature in continuous gas flux mode. Gas was injected into the chamber through a precision leak valve and regulated using a flux controller (1 bar with a gas flux of 50 ml/min). Sensor conductance measurements were normalized by the response recorded without gas under a base pressure around $10^{-2}$ mbar into the chamber. A multimeter from Keithley instruments (Model 6514) was employed to record the resistance measurement applying a bias voltage of 10 V.

## 3. Results

### *3.1. Morphological and structural characterization*

During the growth process by pulsed laser deposition of both $\alpha$-$Fe_2O_3$ and Au layers, in-situ RHEED technique was employed to monitor their crystalline character. From the initial stages of deposition, intense patterns were observed. Figure 1 shows representative RHEED patterns of the clean STO(111) substrate and those of $\alpha$-$Fe_2O_3$ thin film grown on STO(111) and Au islands grown on $\alpha$-$Fe_2O_3$/STO(111) at the final growth stages. In both layers, the RHEED patterns show smooth diffraction stripes, related to homogeneous and crystalline films.

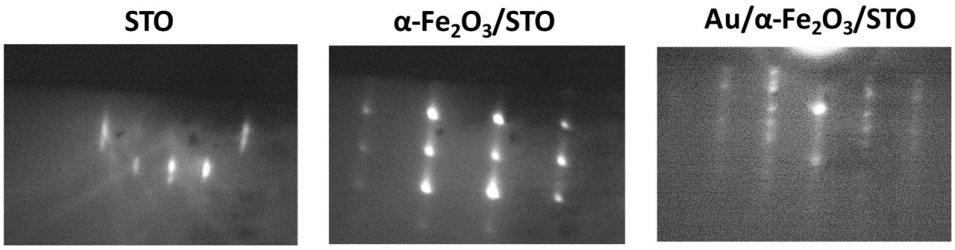


**Figure 1.** Representative RHEED patterns of the clean STO(111) substrate, $\alpha$-$Fe_2O_3$ thin films grown on STO(111) substrate and Au islands grown on $\alpha$-$Fe_2O_3$/STO(111) system. During the deposition process of both $\alpha$-$Fe_2O_3$ and Au layers, intense patterns with smooth diffraction stripes are identified.

Figure 2 shows the SEM images and the particle size distribution analysis for $\alpha$-$Fe_2O_3$ thin film and Au/$\alpha$-$Fe_2O_3$ bilayer prepared on oxide STO(111) substrate. $\alpha$-$Fe_2O_3$ thin film grown on STO(111) (Figure 2a) shows a homogeneous coverage of particles with an average size about 62(2) nm, identifying an island-type growth. The greater interaction of $\alpha$-$Fe_2O_3$ atoms with those of the STO substrate generates the formation of a $\alpha$-$Fe_2O_3$ layer with a nanoparticulated character in order to minimize the system free energy. For the case of the Au/$\alpha$-$Fe_2O_3$ bilayer, a nanostructured top layer related to the formation of Au islands is obtained on $\alpha$-$Fe_2O_3$/STO(111) system. Au islands also show a homogeneous coverage on $\alpha$-$Fe_2O_3$ surface, with an average particle size of 40(2) nm (see Figure 2b). This type of growth is induced during the Au growth when keeping the sample substrate at a temperature of 250 ºC, as was identified previously in [28], inducing an island-type growth of Au that is promoted by the surface diffusion. The phenomenon is attributed to a dewetting process by a one-step procedure [26-28] instead of the usual methodology based on the post-annealing of the metallic film [22–24,29,34]. Specifically, here the $\alpha$-$Fe_2O_3$ surface presents a particulated character with a discontinuous profile which generates a more heterogeneous stress distribution than in a flat surface. These features of the bottom layer favor the nucleration of Au holes and the formation of larger and more separated Au islands in order to minimize the interface energy of the system [35], with qualitative similar final results.

 doi:10.20944/preprints202106.0539.v1



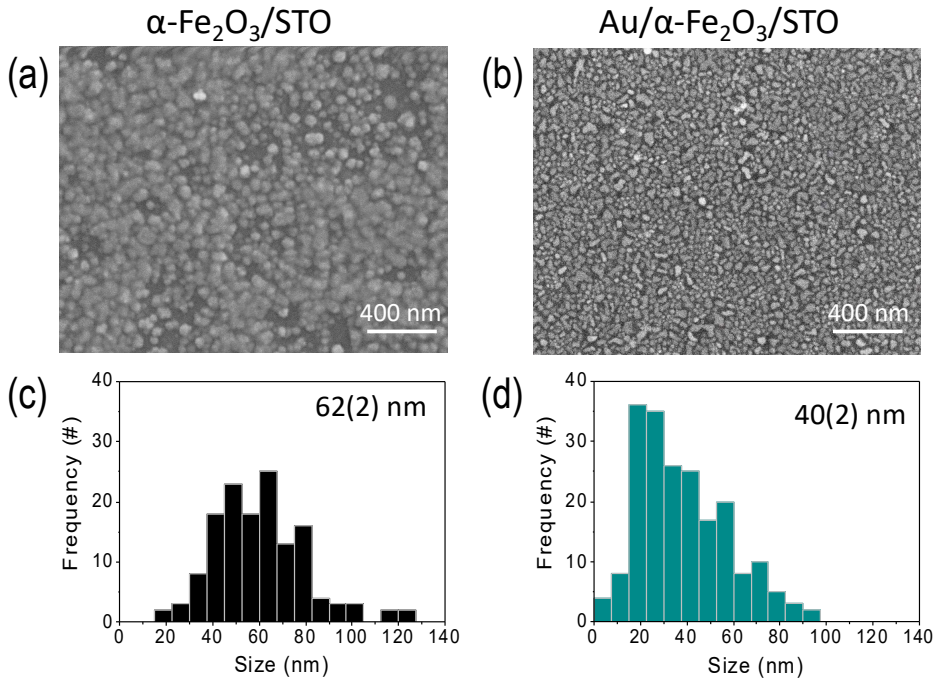


**Figure 2.** (**a,b**) SEM images and (**c,d**) particle size distribution analysis of $\alpha$-$Fe_2O_3$ layer and Au/$\alpha$-$Fe_2O_3$ bilayer grown on STO(111) substrate. An island-type growth for $\alpha$-$Fe_2O_3$ and Au layers is recognized with a homogeneous coverage of particles.

To analyse the in-plane and out-plane crystalline growth of the Au and $\alpha$-$Fe_2O_3$ layer, high resolution GIXRD, XRR and reciprocal space maps (RSM) measurements were performed. From low angle XRR measurements of the $\alpha$-$Fe_2O_3$ layer and Au/$\alpha$-$Fe_2O_3$ bilayer deposited on oxide STO(111), shown in Figure 3a, the thicknesses of the layers were estimated using the period of the oscillations. A thickness of 28(2) nm for the $\alpha$-$Fe_2O_3$ layers and 6(1) nm for the Au layer was obtained. Representative high angle XRR measurements for $\alpha$-$Fe_2O_3$ layer and Au/$\alpha$-$Fe_2O_3$ bilayer grown on STO(111) substrate are shown in Figure 3b. In the $\alpha$-$Fe_2O_3$/STO(111) system, in addition to the difraction peak corresponding to the STO(111) substrate, the presence of $\alpha$-$Fe_2O_3$ with (0001) orientation as single phase is identified, which is not clearly recognized in the difraction pattern of the Au/$\alpha$-$Fe_2O_3$ bilayer. In the case of the Au/$\alpha$-$Fe_2O_3$ bilayer the Au nanostructured layer on top of $\alpha$-$Fe_2O_3$ layer is recognized as a wide peak at lower 2$\theta$ values than the difraction peak related to the $\alpha$-$Fe_2O_3$ layer, which corresponds to epitaxial Au with a (111) orientation and is responsible for masking the difraction peak signal related to the epitaxial $\alpha$-$Fe_2O_3$ layer. It should be pointed out that some Kiessig fringes around layer Bragg peaks can be noted, indicating the occurrence of high quality and smooth surfaces and abrupt $\alpha$-$Fe_2O_3$/STO substrate and Au/$\alpha$-$Fe_2O_3$ interfaces. These results are in agreement with those previously reported in [28].

 doi:10.20944/preprints202106.0539.v1



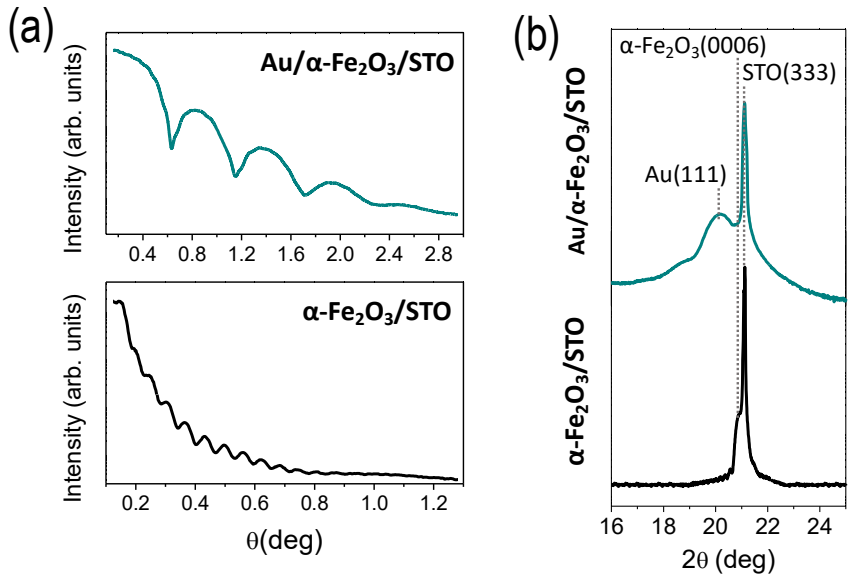


**Figure 3.** (**a**) Low angle XRRs and (**b**) high-angle θ-2θ scans of epitaxial $\alpha$-$Fe_2O_3$ layer and Au/$\alpha$-$Fe_2O_3$ system grown on STO(111) substrate. Thicknesses were calculated to be 28(2) nm for the $\alpha$-$Fe_2O_3$ layers and 6(1) nm for the Au layer. Bragg peaks related to STO(111) substrate, Au(111) and $\alpha$-$Fe_2O_3$(0001) are identified.

Representative RSM measurements for the single $\alpha$-$Fe_2O_3$ layer and Au/$\alpha$-$Fe_2O_3$ bi-layer grown on STO(111) substrate are displayed in Figure 4. Taking into account the analysis of RSM measurements, an incommensurate growth based on the non-coincidence of the in-plane diffraction peak maxima from both Au and $\alpha$-$Fe_2O_3$ layers and the STO substrate is recognized. Besides, the crystallographic coupling between the layers and the substrate is analyzed. A rotation of 30º is shown between the in-plane crystallographic axes of the $\alpha$-$Fe_2O_3$ layer and the STO(111) substrate and the Au layer and the $\alpha$-$Fe_2O_3$ layer, with the crystallographic axes between Au and STO substrate parallel. Thus, the orientation relationships between the lattices of Au and $\alpha$-$Fe_2O_3$ layers and the STO substrate is: $(0001)[100]_{\alpha\text{-}Fe2O3} \,||\, (111)[110]_{STO}$ for $\alpha$-$Fe_2O_3$/STO(111) and $(111)[110]_{Au} \,||\, (0001)[100]_{\alpha\text{-}Fe2O3} \,||\, (111)[110]_{STO}$ for Au/$\alpha$-$Fe_2O_3$/STO(111) system, as previously reported [28,36].

Out-of-plane and in-plane lattice parameters were calculated from the positions at several diffraction peaks in reciprocal space respect to the STO(111) substrate obtaining for $\alpha$-$Fe_2O_3$ layers: $c_{\alpha\text{-}Fe2O3/STO} = 13.72(6)$ Å, $c_{Au/\alpha\text{-}Fe2O3/STO} = 13.72(3)$ Å, $a_{\alpha\text{-}Fe2O3} = b_{\alpha\text{-}Fe2O3} = 5.08(4)$ Å and $a_{Au/\alpha\text{-}Fe2O3/STO} = b_{Au/\alpha\text{-}Fe2O3/STO} = 5.07(1)$ Å and for Au layer: $c_{Au/\alpha\text{-}Fe2O3/STO} = 7.04(2)$ Å and $a_{Au/\alpha\text{-}Fe2O3/STO} = b_{Au/\alpha\text{-}Fe2O3/STO} = 2.89(2)$ Å. Additionally, the in-plane domain sizes were calculated to be around 25 nm for the epitaxial $\alpha$-$Fe_2O_3$ layer and Au/$\alpha$-$Fe_2O_3$ system and around 17 nm for the epitaxial Au, in agreement with a previous work [28]. Similar values of both the lattice crystallographic parameters and in-plane domain size are obtained in the $\alpha$-$Fe_2O_3$ layer before and after the deposition of Au islands, indicanding the no crystallographic alterations of the iron oxide structure and its stability during the Au growth at 250 ºC. Besides, lattice parameters match those of the bulk $\alpha$-$Fe_2O_3$ structure disclosing a stress-free growth of layers.

Preprints (www.preprints.org) | NOT PEER-REVIEWED | Posted: 22 June 2021 doi:10.20944/preprints202106.0539.v1



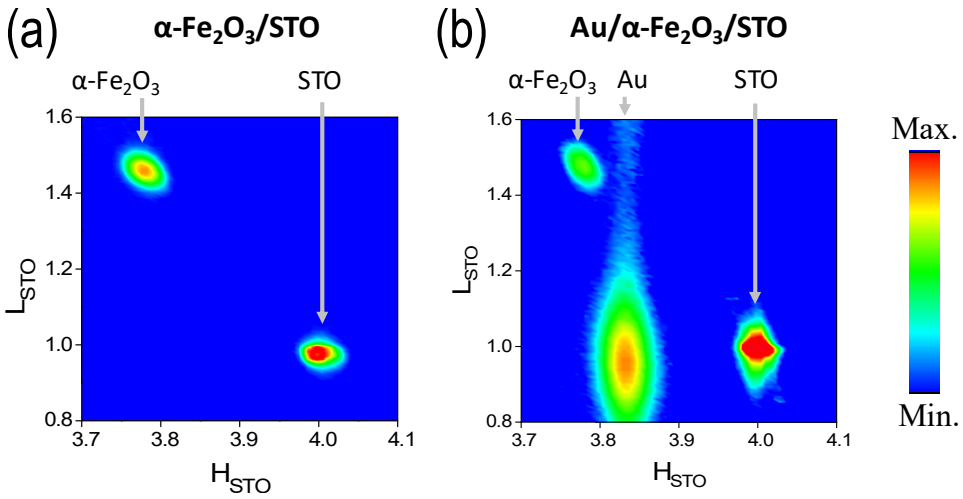


**Figure 4.** LH reciprocal space maps (RSM) for (a) $\alpha$-$Fe_2O_3$ layer grown on STO(111) substrate and (b) Au/$\alpha$-$Fe_2O_3$ bilayer prepared on STO(111) substrate. An incommensurate epitaxial growth is identified from a non-coincidence of Au(111), $\alpha$-$Fe_2O_3$(0001) and STO(111) substrate in-plane peaks (marked in each Figure). The colour scale corresponds to the signal intensity.

Possible $\alpha$-$Fe_2O_3$ modifications at short-range order during the growth of Au nanoparticles or other amorphous minority phases non identified by GIXRD are analyzed by XAS experiments, as Figure 5 shows. Both X-ray absorption near-edge structure (XANES) and extended X-ray absorption fine structure (EXAFS) measurements were achieved. Absorption profiles obtained by XANES measurements at the Fe K-edge of heterostructures follow the absorption features of powder $\alpha$-$Fe_2O_3$ reference (see Figure 5a). Fitting the XANES spectra by a linear combination of different iron oxide reference compounds (Fe, FeO, $Fe_3O_4$ and $\alpha$-$Fe_2O_3$ references)[37,38][paper CSP SFOAAG] (not shown) confirms an oxidation state of Fe3+ and a 100 % of $\alpha$-$Fe_2O_3$ phase in both $\alpha$-$Fe_2O_3$ layer and Au/ $\alpha$-$Fe_2O_3$ bilayer grown on STO(111) substrate, corroborating the $\alpha$-$Fe_2O_3$ phase as single iron oxide phase before and after the deposition of Au islands.

The short-range ordering of cations around the Fe is studied in both $\alpha$-$Fe_2O_3$ layer and Au/$\alpha$-$Fe_2O_3$ bilayer by EXAFS spectroscopy. Figure 5b shows the modulus of the Fourier transform (FT) of the EXAFS signal at the Fe K-edge. The FT is performed in the $k^2\chi(k)$ weighted EXAFS signal between 2.5 and 10.5 $Å^{-1}$. Experimental EXAFS results were fitted in R-space in the range 1.0-3.6 Å using the FEFFIT code [31]. The first intense peak involves two subshells that corresponds to a first neighbor shell with three short plus three long O neighbors around the Fe and the second peak is related to single and multiple scatterings from the nearest Fe-Fe neighbors [39]. The fitting was performed fixing the shift at the edge energy $E_0$, which was previously calculated from $\alpha$-$Fe_2O_3$ powder reference, and the coordination number N, the interatomic distance R and the Debye-Waller (DW) factors $\sigma^2$ were used as free parameters for the fitting. Table 1 shows the parameters obtained from the EXAFS fittings.

Preprints (www.preprints.org) | NOT PEER-REVIEWED | Posted: 22 June 2021 doi:10.20944/preprints202106.0539.v1



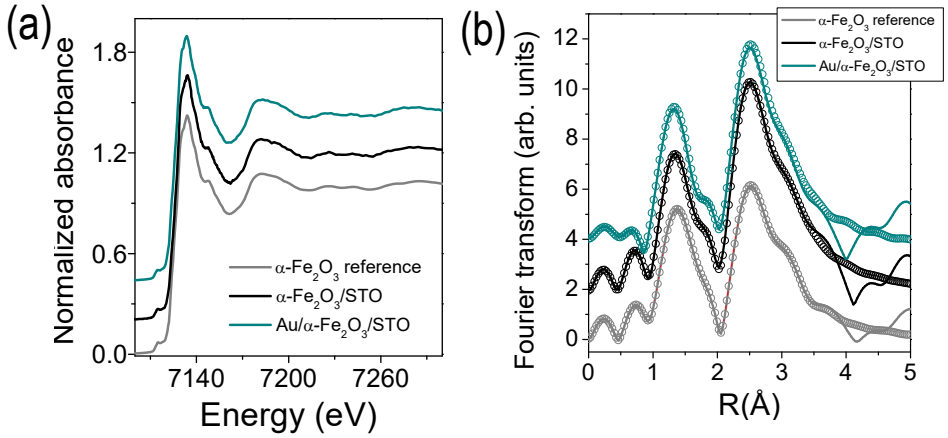


**Figure 5.** (**a**) XANES spectra and (**b**) modulus of the FT of the EXAFS signal (lines with symbols) and best-fitting simulations (continuous lines) at the Fe K-absorption edge energy of $\alpha$-$Fe_2O_3$ layer and Au/$\alpha$-$Fe_2O_3$ bilayer grown on STO(111). XANES spectum and FT of the EXAFS signal of $\alpha$-$Fe_2O_3$ powder reference is presented for comparison.

**Table 1.** Results of the EXAFS fittings by a five-shell model at the Fe-K edge of $\alpha$-$Fe_2O_3$ layer and Au/$\alpha$-$Fe_2O_3$ bilayer grown on STO(111). EXAFS parameters are compared with results obtained from powder $\alpha$-$Fe_2O_3$ reference.

| Sample | shell | N | R (Å) | DW(Å²) |
|---|---|---|---|---|
| **α-$Fe_2O_3$ reference** | **Fe-O1** | 3 | 1.967(4) | 0.006(1) |
| | **Fe-O2** | 3 | 2.13(1) | 0.017(2) |
| | **Fe-Fe1** | 1 | 2.977(1) | 0.006(1) |
| | **Fe-Fe2** | 3 | 3.06(1) | 0.007(1) |
| | **Fe-Fe3** | 3 | 3.454(1) | 0.017(1) |
| **α-$Fe_2O_3$/STO** | **Fe-O1** | 3.4(2) | 1.981(8) | 0.003(1) |
| | **Fe-O2** | 3.4(2) | 2.188(3) | 0.014(1) |
| | **Fe-Fe1** | 1.2(1) | 2.90(4) | 0.032(9) |
| | **Fe-Fe2** | 3.6(3) | 2.983(2) | 0.003(1) |
| | **Fe-Fe3** | 3.6(3) | 3.380(2) | 0.005(1) |
| **Au/α-$Fe_2O_3$/STO** | **Fe-O1** | 3.7(2) | 1.993(6) | 0.003(1) |
| | **Fe-O2** | 3.7(2) | 2.230(5) | 0.013(2) |
| | **Fe-Fe1** | 1.2(1) | 2.82(6) | 0.032(9) |
| | **Fe-Fe2** | 3.6(3) | 3.001(3) | 0.004(2) |
| | **Fe-Fe3** | 3.6(3) | 3.394(4) | 0.005(1) |

In both $\alpha$-$Fe_2O_3$/STO(111) and Au/$\alpha$-$Fe_2O_3$/STO(111) systems, $\alpha$-$Fe_2O_3$ layer presents an increase of the coordination number at the five coordination shells with respect to the $\alpha$-$Fe_2O_3$ reference (see Table 1) that can be related to the greatest local order in the epitaxial thin films. With respect to the neighbor bondlengths, both $\alpha$-$Fe_2O_3$ layers (single and with Au islands) presents an Fe-O elongation and Fe-Fe contraction, indicating a local distortion at short-range order of epitaxial $\alpha$-$Fe_2O_3$ structure grown on STO(111) substrate in comparison with the $\alpha$-$Fe_2O_3$ reference. Specifically, for Au/$\alpha$-$Fe_2O_3$/STO(111) system most of first neighbors presents slightly larger bondlength distances than for $\alpha$-$Fe_2O_3$/STO(111), which supposes a short-range order expansion that could be related to a relaxion of the $\alpha$-$Fe_2O_3$ structure promoted as the Au islands are deposited on $\alpha$-$Fe_2O_3$(0001)/STO(111) system with the substrate at a certain temperature (250 ºC). Finally, the obtained DW factors are of similar order for both $\alpha$-$Fe_2O_3$(0001) layers and we do not observe a structural disorder related to the growth of Au island adlayer.

Preprints (www.preprints.org) | NOT PEER-REVIEWED | Posted: 22 June 2021 doi:10.20944/preprints202106.0539.v1



The incorporation of Au islands on $\alpha$-$Fe_2O_3$/STO(111) was also investigated by XPS measurements on the Fe 2p and Au 4f core level, as Figure 6 shows. The binding energy values of the Fe $2p_{3/2}$ peak (~710 eV) and the Fe $2p_{1/2}$ peak (~723.6 eV), with a distance among both of around 13.6 eV, were determinated to be similar in both $\alpha$-$Fe_2O_3$ layer and Au/$\alpha$-$Fe_2O_3$ bilayer and similar to typical values reported for Fe 2p a-$Fe_2O_3$ [40–42]. In addition, the satellite peak of Fe $2p_{3/2}$ is distinguished, most clearly in the $\alpha$-$Fe_2O_3$/STO(111) sample, and located around 8 eV higher than the main Fe $2p_{3/2}$ peak [40–42]. These results confirm the oxidation state of the Fe cations to be Fe3+ and the nature of iron oxide layer as $\alpha$-$Fe_2O_3$, in agreement to GIXRD and XAS results. During the XPS measurements, a lower signal is collected on the Fe 2p core level for the Au/$\alpha$-$Fe_2O_3$ bilayer than for $\alpha$-$Fe_2O_3$ layer due to the presence of Au islands. The Fe 2p signal is very low since the $\alpha$-$Fe_2O_3$ is buried 6 nm (Au layer thickness), which is approximately the depth limit of conventional XPS (see Figure 2). On the Au 4f core level, photoemission signal related to Au/$\alpha$-$Fe_2O_3$ bilayer grown on STO(111) substrate shows a spin-orbit splitting of 3.7 eV between Au $4f_{5/2}$ and Au $4f_{7/2}$ peaks and an intensity relationship corresponding to that of pure Au [43,44]. Moreover, the Fe 3s signal is imperceptible with respect to that of Au 4f, which means that the nanostructured-Au layer is homogeneous and there is not segregation of Fe by the Au layer. The combination of XPS and XANES demonstrates the absence of mixed Fe-Au phases present on the surface and buried interfaces.

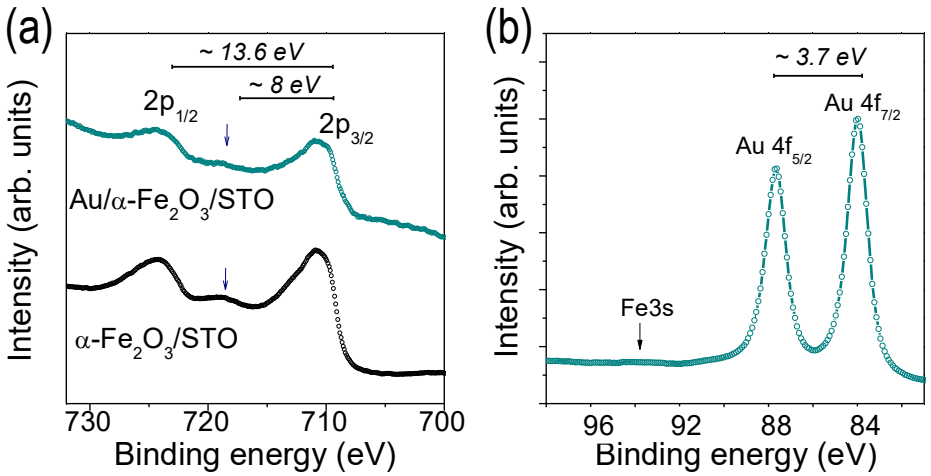


**Figure 6.** XPS measurements on the (**a**) Fe 2p core level of $\alpha$-$Fe_2O_3$ layer and Au/$\alpha$-$Fe_2O_3$ bilayer grown on STO(111) and (**b**) Au 4f core level of Au/$\alpha$-$Fe_2O_3$ bilayer grown on STO(111). Lower signal is collected on the Fe 2p core level for the Au/$\alpha$-$Fe_2O_3$ bilayer than for $\alpha$-$Fe_2O_3$ layer.

### *3.2. Conductance response*

The sensibility of the $\alpha$-$Fe_2O_3$ layer and Au/$\alpha$-$Fe_2O_3$ complex bilayer as gas sensing under CO and $CH_4$ atmospheres at room temerature is shown in Figure 7. For that, the relative conductance response ($\Delta G/G_0$) of the Au/$\alpha$-$Fe_2O_3$ complex system is compared in each case with the results obtained for the single $\alpha$-$Fe_2O_3$ layer deposited on STO(111) substrate under the same conditions. $\alpha$-$Fe_2O_3$ is a n-type semiconductor and its gas response involves the formation of an electron depletion layer at the surface and the return of these electrons to the conduction band, increasing the conductance signal after exposure to reducing gases [15,18,45].

On $\alpha$-$Fe_2O_3$/STO(111) in contact with air, oxygen molecules are adsorbed at the $\alpha$-$Fe_2O_3$ surface. When the gas passes through the $\alpha$-$Fe_2O_3$ surface, it is chemisorbed at the surface with previously adsorbed oxygen and an oxidation reaction occurs. So, the trapped electrons on the surface are released back to the conduction band producing an

 doi:10.20944/preprints202106.0539.v1



increase of the electrical conductance of $\alpha$-$Fe_2O_3$, as shown in Figure 7 for the measurements performed at room temperature. Prior to the experiments, the linear behavior of the resistance signal was checked in each sample.

As the $\alpha$-$Fe_2O_3$ is functionalized on top with Au islands, Au/$\alpha$-$Fe_2O_3$ complex bilayer, the gas sensor sensibility increases around 25% under CO gas and around 35% under $CH_4$ (see Figure 7), which should be ascribed to the active Au islands that play an important role in catalyzing the surface sensing reactions [12,21]. It should be noted that in both on Au/$\alpha$-$Fe_2O_3$ complex bilayer and single $\alpha$-$Fe_2O_3$ layer, the sensor response for the $CH_4$ is higher than for the CO gas (~5-10 %).

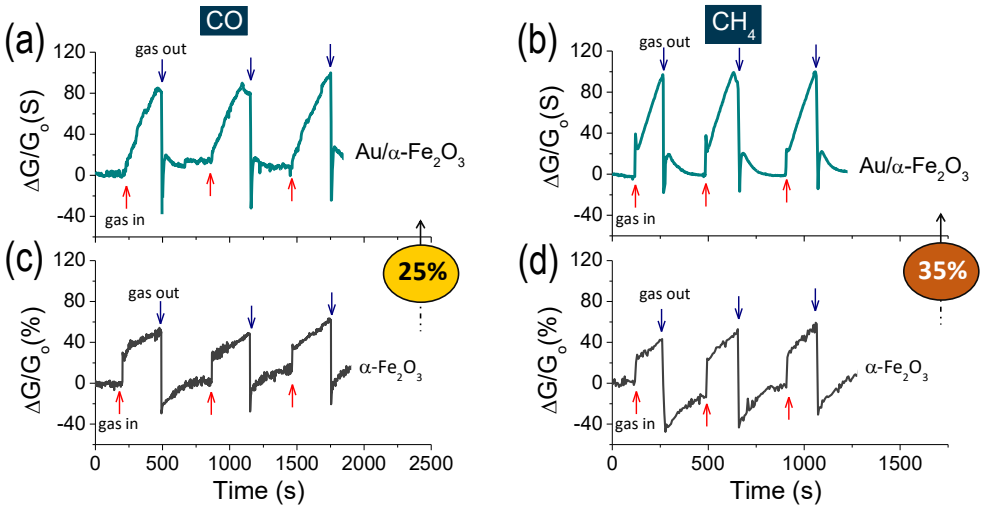


**Figure 7.** Gas sensor response curves for (a, b) Au/$\alpha$-$Fe_2O_3$ bilayers deposited on STO(111) substrate at a substrate temperature for the Au growth of 250 ºC and (c, d) bare $\alpha$-$Fe_2O_3$ thin film under (a, c) CO and (b,d) $CH_4$ atmosphere at room temperature. $G_0$ and G values correspond to the sensor conductance in air and specific gas atmosphere.

Therefore, these results are very promising for gas sensor applications at room temperature where the incorporation of epitaxial Au(111) islands on epitaxial $\alpha$-$Fe_2O_3$(0001) layers grown on STO(111) substrates improves the gas sensor response, in addition exhibiting plasmonic activity as previously reported [28] and demostrating the multifnctional character of these hybrid Au/$\alpha$-$Fe_2O_3$ systems.

## 5. Conclusions

We have grown epitaxial incommensurate $\alpha$-$Fe_2O_3$(0001) layers and Au(111)/ $\alpha$-$Fe_2O_3$ (0001) bilayers on STO(111) substrates by pulsed layer deposition with CO and $CH_4$ gas sensor response at room temperature, identifying the influence of the incorporation of Au nanostructures in the physical properties of $\alpha$-$Fe_2O_3$ structure. An island-type growth is recognized in both Au and $\alpha$-$Fe_2O_3$. Structurally, both before and after the Au deposition, $\alpha$-$Fe_2O_3$ is the single iron oxide phase identified with a slight increase in the coordination number and variations in the neighbor bondlengths at short-range order. The epitaxial growth is confirmed, with the in-plane crystallographic axes between Au and $\alpha$-$Fe_2O_3$ and those between $\alpha$-$Fe_2O_3$ and STO(111) rotated 30º. Gas sensor response under CO and $CH_4$ atmosphere is measured at room temperature in both $\alpha$-$Fe_2O_3$/STO(111) and Au(111)/ $\alpha$-$Fe_2O_3$(0001)/STO(111) systems, being higher for the $CH_4$ gas and obtaining an improved gas-sensing activity as the $\alpha$-$Fe_2O_3$(0001) surface is functionalized with Au nanostructures.

**Author Contributions:** Conceptualization, methodology, investigation, formal analysis, data curation, writing—original draft and funding acquisition, A.S.; investigation, formal analysis and review—editing, J.L.-S., I.A, R.C, M.V. and E.S.-C.; methodology, investigation, supervision, review—

editing and funding acquisition, G.R.C. and J.R-Z. All authors have read and agreed to the published version of the manuscript.

**Funding and acknowledgments:** This work has been supported by the Ministerio Español de Ciencia, Innovación y Universidades (MCIU) and the Consejo Superior de Investigaciones Cientificas (CSIC) through the projects PIE-2010-OE-013-200014, PIE 2021-60-E-030 and RTI2018-095303-A-C52. The ESRF, MCIU and CSIC are acknowledged for the provision of synchrotron radiation facilities. A.S. acknowledges financial support from Comunidad de Madrid for an "Atracción de Talento Investigador" Contract (2017-t2/IND5395). We especially thank Carlos Beltrán for his technical support during the experiments at the BM25 beamline at The ESRF.

## References

1. Mishra, M.; Chun, D.M. α-Fe2O3 as a photocatalytic material: A review. *Appl. Catal. A Gen.* **2015**, *498*, 126–141, doi:10.1016/j.apcata.2015.03.023.
2. Mirzaei, A.; Hashemi, B.; Janghorban, K. α-Fe2O3 based nanomaterials as gas sensors. *J. Mater. Sci. Mater. Electron.* **2016**, *27*, 3109–3144, doi:10.1007/s10854-015-4200-z.
3. Ali, A.; Zafar, H.; Zia, M.; ul Haq, I.; Phull, A.R.; Ali, J.S.; Hussain, A. Synthesis, characterization, applications, and challenges of iron oxide nanoparticles. *Nanotechnol. Sci. Appl.* **2016**, *9*, 49–67, doi:10.2147/NSA.S99986.
4. Khatavkar, S.N.; Sartale, S.D. α-Fe2O3 thin films by liquid phase deposition: low-cost option for supercapacitor. *J. Solid State Electrochem.* **2017**, *21*, 2555–2566, doi:10.1007/s10008-016-3457-3.
5. Cornell, R.M.; Schwertmann, U. *The Iron Oxides: Structure, Properties, Reactions, Occurrence and Uses*; 2nd edition WILEY-VCH Verlag GmbH & Co. KGaA, Weinheim, 2003;
6. Liang, H.; Jiang, X.; Qi, Z.; Chen, W.; Wu, Z.; Xu, B.; Wang, Z.; Mi, J.; Li, Q. Hematite concave nanocubes and their superior catalytic activity for low temperature CO oxidation. *Nanoscale* **2014**, *6*, 7199, doi:10.1039/c4nr00552j.
7. Yan, S.; Wu, Q. A novel structure for enhancing the sensitivity of gas sensors - α-Fe2O3 nanoropes containing a large amount of grain boundaries and their excellent ethanol sensing performance. *J. Mater. Chem. A* **2015**, *3*, 5982–5990, doi:10.1039/c4ta06861k.
8. Marti, X.; Fina, I.; Jungwirth, T. Prospect for antiferromagnetic spintronics. *IEEE Trans. Magn.* **2015**, *51*, 18–21, doi:10.1109/TMAG.2014.2358939.
9. Zeng, L.; Li, K.; Wang, H.; Yu, H.; Zhu, X.; Wei, Y.; Ning, P.; Shi, C.; Luo, Y. CO Oxidation on Au/α-Fe2O3-Hollow Catalysts: General Synthesis and Structural Dependence. *J. Phys. Chem. C* **2017**, *121*, 12696–12710, doi:10.1021/acs.jpcc.7b01363.
10. Shen, S.; Lindley, S.A.; Chen, X.; Zhang, J.Z. Hematite heterostructures for photoelectrochemical water splitting: Rational materials design and charge carrier dynamics. *Energy Environ. Sci.* **2016**, *9*, 2744–2775, doi:10.1039/c6ee01845a.
11. Schultz, A.M.; Salvador, P. a.; Rohrer, G.S. Enhanced photochemical activity of α-Fe2O3 films supported on SrTiO3 substrates under visible light illumination. *Chem. Commun.* **2012**, *48*, 2012, doi:10.1039/c2cc16715h.
12. Garcia, D.; Picasso, G.; Hidalgo, P.; Peres, H.E.M.; Sun Kou, R.; Gonçalves, J.M. Sensors based on Ag-loaded hematite (α-Fe2O3) nanoparticles for methyl mercaptan detection at room temperature. *Anal. Chem. Res.* **2017**, *12*, 74–81, doi:10.1016/j.ancr.2016.12.001.
13. Aronniemi, M.; Lahtinen, J.; Hautojärvi, P. Characterization of iron oxide thin films. *Surf. Interface Anal.* **2004**, *36*, 1004–1006, doi:10.1002/sia.1823.
14. Mirzaeian, M.; Ogwu, A.A.; Jirandehi, H.F.; Aidarova, S.; Ospanova, Z.; Tsendzughul, N. Surface characteristics of silver oxide thin film electrodes for supercapacitor applications. *Colloids Surfaces A Physicochem. Eng. Asp.* **2017**, *519*, 223–230, doi:10.1016/j.colsurfa.2016.04.026.
15. Wang, L.; Lou, Z.; Deng, J.; Zhang, R.; Zhang, T. Ethanol Gas Detection Using a Yolk-Shell (Core-Shell) α-Fe<inf>2</inf>O<inf>3</inf> Nanospheres as Sensing Material. *ACS Appl. Mater. Interfaces* **2015**, *7*, 13098–13104, doi:10.1021/acsami.5b03978.
16. Cuong, N.D.; Hoa, T.T.; Khieu, D.Q.; Hoa, N.D.; Van Hieu, N. Gas sensor based on nanoporous hematite nanoparticles: Effect of synthesis pathways on morphology and gas sensing properties. *Curr. Appl. Phys.* **2012**, *12*, 1355–1360, doi:10.1016/j.cap.2012.03.026.
17. Li, X.; Wei, W.; Wang, S.; Kuai, L.; Geng, B. Single-crystalline α-Fe2O3 oblique nanoparallelepipeds: High-yield synthesis, growth mechanism and structure enhanced gas-sensing properties. *Nanoscale* **2011**, *3*, 718–724, doi:10.1039/c0nr00617c.
18. Hung, C.M.; Hoa, N.D.; Van Duy, N.; Van Toan, N.; Le, D.T.T.; Van Hieu, N. Synthesis and gas-sensing characteristics of α-Fe2O3hollow balls. *J. Sci. Adv. Mater. Devices* **2016**, *1*, 45–50, doi:10.1016/j.jsamd.2016.03.003.
19. Wang, L.; Wang, L.; Hu, H.; Truong, N.; Zhang, Y.; Schmuki, P.; Bi, Y. Plasmon-Induced Hole-Depletion Layer on Hematite Nanoflake Photoanodes for Highly Efficient Solar Water Splitting Nano Energy Plasmon-induced hole-depletion layer on hematite nano fl ake photoanodes for highly e ffi cient solar water splitting. *Nano Energy* **2017**, *35*, 171–178, doi:10.1016/j.nanoen.2017.03.035.
20. Gao, H.; Liu, C.; Jeong, H.E.; Yang, P. Plasmon-enhanced photocatalytic activity of iron oxide on gold nanopillars. *ACS Nano* **2012**, *6*, 234–40, doi:10.1021/nn203457a.

21. Zhang, J.; Liu, X.; Wang, L.; Yang, T.; Guo, X.; Wu, S.; Wang, S.; Zhang, S. Au-functionalized hematite hybrid nanospindles: General synthesis, gas sensing and catalytic properties. *J. Phys. Chem. C* **2011**, *115*, 5352–5357, doi:10.1021/jp110421v.
22. Thompson, C. V Solid-State Dewetting of Thin Films. *Annu. Rev. Mater. Res.* **2012**, *42*, 399–434, doi:10.1146/annurev-matsci-070511-155048.
23. Leroy, F.; Borowik, Ł.; Cheynis, F.; Almadori, Y.; Curiotto, S.; Trautmann, M.; Barbe, J.C.; Müller, P. How to control solid state dewetting: A short review. *Surf. Sci. Rep.* **2016**, *71*, 391–409, doi:10.1016/j.surfrep.2016.03.002.
24. Serrano, A.; De La Fuente, O.R.; García, M.A. Extended and localized surface plasmons in annealed Au films on glass substrates. *J. Appl. Phys.* **2010**, *108*, doi:10.1063/1.3485825.
25. Serrano, A.; Fernandez, J.F.; Rodriguez de la Fuente, O.; García, M.A. A novel route to obtain metal and oxide nanoparticles co-existing on a substrate. *Mater. Today Chem.* **2017**, *4*, 64–72, doi:10.1016/j.mtchem.2017.02.005.
26. Gatel, C.; Snoeck, E. Epitaxial growth of Au and Pt on Fe3O4(1 1 1) surface. *Surf. Sci.* **2007**, *601*, 1031–1039, doi:10.1016/j.susc.2006.11.045.
27. Lachebi, I.; Fedala, A.; Djenizian, T.; Hadjersi, T.; Kechouane, M. Morphological and optical properties of aluminum nanoparticles deposited by thermal evaporation on heated substrates. *Surf. Coatings Technol.* **2018**, *343*, 160–165, doi:10.1016/j.surfcoat.2017.09.061.
28. Serrano, A.; Rubio-Zuazo, J.; López-Sánchez, J.; Enríquez, E.; Salas-Cólera, E.; Castro, G.R. Nanostructured Au(111)/Oxide Epitaxial Heterostructures with Tailoring Plasmonic Response by a One-Step Strategy. *J. Phys. Chem. C* **2019**, *123*, 25294–25302, doi:10.1021/acs.jpcc.9b04768.
29. Serrano, A.; Llorca-Hernando, O.; Del Campo, A.; Rubio-Marcos, F.; Rodríguez de La Fuente, O.; Fernández, J.F.; García, M.A. Ag-AgO nanostructures on glass substrates by solid-state dewetting: From extended to localized surface plasmons. *J. Appl. Phys.* **2018**, *124*, doi:10.1063/1.5049651.
30. Rubio-zuazo, J.; Ferrer, P.; López, A.; Gutiérrez-león, A.; Silva, I.; Castro, G.R. Nuclear Instruments and Methods in Physics Research A The multipurpose X-ray diffraction end-station of the BM25B-SpLine synchrotron beamline at the ESRF. *Nucl. Inst. Methods Phys. Res. A* **2013**, *716*, 23–28, doi:10.1016/j.nima.2013.03.019.
31. Newville, M.; Ravel, B.; Haskel, D.; Rehra, J.J.; Stern, E.A.; Yacoby, Y. Analysis of multiple-scattering XAFS data using theoretical standards. *Phys. B Condens. Matter* **1995**, *208--209*, 154–156, doi:10.1016/0921-4526(94)00655-F.
32. Ravel, B.; Newville, M. ATHENA , ARTEMIS , HEPHAESTUS : data analysis for X-ray absorption spectroscopy using IFEFFIT. *J. Synchrotron Radiat.* **2005**, *12*, 537–541, doi:10.1107/S0909049505012719.
33. Lachebi, I.; Fedala, A.; Djenizian, T.; Hadjersi, T.; Kechouane, M. Morphological and optical properties of aluminum nanoparticles deposited by thermal evaporation on heated substrates. *Surf. Coatings Technol.* **2018**, *343*, 160–165, doi:10.1016/j.surfcoat.2017.09.061.
34. Sharma, S.K.; Spitz, J. Hillock formation, hole growth and agglomeration in thin silver films. *Thin Solid Films* **1980**, *65*, 339–350, doi:10.1016/0040-6090(80)90244-8.
35. Serrano Rubio, A. *Modified Au-Based Nanomaterials Studied by Surface Plasmon Resonance Spectroscopy*; Springer Theses, 2015;
36. Serrano, A.; Rubio-Zuazo, J.; López-Sánchez, J.; Arnay, I.; Salas-Colera, E.; Castro, G.R. Stabilization of Epitaxial α-Fe<inf>2</inf>O<inf>3</inf> Thin Films Grown by Pulsed Laser Deposition on Oxide Substrates. *J. Phys. Chem. C* **2018**, *122*, doi:10.1021/acs.jpcc.8b02430.
37. Rubio-Zuazo, J.; Onandia, L.; Salas-Colera, E.; Mu??oz-Noval, A.; Castro, G.R. Incommensurate growth of thin and ultrathin films of single-phase Fe3O4(001) on SrTiO3(001). *J. Phys. Chem. C* **2015**, *119*, 1108–1112, doi:10.1021/jp510615j.
38. Malferrari, D.; Castellini, E.; Bernini, F.; Rubio, A.S.; Castro, G.R.; Sainz-Díaz, C.I.; Caleffi, M.; Brigatti, M.F.; Borsari, M. Chemical trapping of gaseous H2S at high and low partial pressures by an iron complex immobilized inside the montmorillonite interlayer. *Microporous Mesoporous Mater.* **2018**, *265*, 8–17, doi:10.1016/j.micromeso.2018.01.017.
39. Sanson, a; Mathon, O.; Pascarelli, S. Local vibrational dynamics of hematite ($\alpha$-$Fe_2O_3$) studied by extended x-ray absorption fine structure and molecular dynamics. *J. Chem. Phys.* **2014**, *140*, 224504, doi:10.1063/1.4882282.
40. Oku, M.; Wagatsuma, K.; Matsuta, H. Background subtraction from transition metal 2p XPS by deconvolution using ligand atom XPS: Study on first transition metal cyanide complexes. *J. Electron Spectros. Relat. Phenomena* **1997**, *83*, 31–39, doi:10.1016/S0368-2048(96)03075-7.
41. Mills, P.; Sullivan, J.L. A study of the core level electrons in iron and its three oxides by means of X-ray photoelectron spectroscopy. *J. Phys. D. Appl. Phys.* **1983**, *16*, 723–732, doi:10.1088/0022-3727/16/5/005.
42. Yamashita, T.; Hayes, P. Analysis of XPS spectra of Fe 2+ and Fe 3+ ions in oxide materials. *Appl. Surf. Sci.* **2008**, *254*, 2441–2449, doi:10.1016/j.apsusc.2007.09.063.
43. Kruse, N.; Chenakin, S. XPS characterization of Au/TiO2 catalysts: Binding energy assessment and irradiation effects. *Appl. Catal. A Gen.* **2011**, *391*, 367–376, doi:10.1016/j.apcata.2010.05.039.
44. Strohmeier, B.R. Copper/Silver/Gold Alloy by XPS. *Surf. Sci. Spectra* **1994**, *3*, 175–181, doi:10.1116/1.1247744.
45. Široký, K.; Jirešová, J.; Hudec, L.L.; Sirok, K.; Jire, J. Iron oxide thin film gas sensor. *Thin Solid Films* **1994**, *245*, 211–214, doi:http://dx.doi.org/10.1016/0040-6090(94)90902-4.